Climate Dynamics (2020) 54:1217–1231
https://doi.org/10.1007/s00382-019-05054-y

Two-way interactions between MJO and high-frequency waves over the Maritime Continent in MJOTF/GASS models

Yan Zhu[1,2] · **Tim Li**[1,2]

Received: 2 July 2019 / Accepted: 11 November 2019 / Published online: 21 November 2019

Abstract
The two-way interaction between the Madden–Julian Oscillation (MJO) and high-frequency waves (HFW) over the Maritime Continent is investigated through the diagnosis of 12 MJOTF/GASS models. The models are divided into good and poor groups based on their performance in capturing the eastward propagation of MJO. Regarding to the modulation of MJO to HFW, it is noted that there is a significant increase (decrease) of HFW intensity over and to the west (east) of MJO convection in the good model group, similar to the observed. However, enhanced HFW appears only over the MJO convective center in the poor model group. The difference in MJO modulation lies in the wind shear and specific humidity patterns associated with the MJO. The upscale feedback of HFW to MJO is investigated through the diagnosis of both anomalous condensational heating ($\tilde{Q}_2$) and eddy momentum transport. It is found that shallow convection associated with $\tilde{Q}_2$ develops in front of MJO deep convection in the good model group, as in observations. The primary contributor to $\tilde{Q}_2$ among the nonlinear rectification of HFW is the meridional advection of specific humidity anomaly ($\widetilde{-Lv'\frac{\partial q'}{\partial y}}$). The zonally asymmetric nonlinear advection is not seen in the poor model group. The contribution from the nonlinear rectification of HFW ($\widetilde{termA}$) to MJO zonal wind tendency is maximum at 850-hPa and similar in the good and poor model groups because of the significant increased HFW over the MJO convection region in both groups. No eastward propagation of the MJO zonal wind in the poor model group attributes to the MJO flows itself.

Keywords Madden–Julian oscillation · High frequency waves · MJOTF/GASS models · Two-way interactions

1 Introduction

Madden Julian Oscillation (MJO; Madden and Julian 1971, 1972), the dominant mode of the intraseasonal variability in the tropics, does not appear as an isolated intraseasonal phenomenon of intraseasonal time scale but interacts with other weather and climate systems of various temporal and spatial scales throughout its life cycle. The MJO convection and the associated flows can modulate the diurnal rainfall over the Maritime Continent (MC) (Rauniyar and Walsh 2011; Oh et al. 2012; Peatman et al. 2014) and generate the intraseasonal variation of the precipitation in the extratropics (Jeong et al. 2008; Wheeler et al. 2009). The intraseasonal variations of the frequency and intensity of tropical cyclones are found to be connected to the MJO activities (Sobel and Maloney 2000; Hall et al. 2001; Klotzbach 2014). The northward-propagating MJO in the boreal summer can change the rainfall variabilities of the Asian summer monsoon (Singh et al.1992; Hung and Yanai 2004; Pai et al. 2011; Grimm 2019). In addition, the surface westerly anomalies associated with the MJO are considered to be a vital source in triggering the downwelling Kelvin waves that related to the onset of *El Niño* (Lengaigne et al. 2003; Hendon et al. 2007; Gushchina and Dewitte 2012; Chiodi et al. 2014; Chen et al. 2016). Besides the interactions with various atmospheric variabilities, the convective envelope of the MJO itself is considered as a hierarchical structure comprised of super

✉ Yan Zhu
yanzhu@hawaii.edu

[1] Key Laboratory of Meteorological Disaster, Ministry of Education (KLME)/Joint International Research Laboratory of Climate and Environmental Change (ILCEC)/ Collaborative Innovation Center on Forecast and Evaluation of Meteorological Disasters (CIC-FEMD), Nanjing University of Information Science and Technology, Nanjing, China

[2] Department of Atmospheric Sciences, and School of Ocean and Earth Science and Technology, University of Hawaii at Manoa, Honolulu, HI, USA

cloud clusters with multiple scales that move either eastward or westward (Nakazawa 1988). The eastward propagating super cloud clusters comprise of convective coupled Kelvin waves (CCKWs), and the westward propagating super cloud clusters consist of mixed Rossby-gravity waves (MRG) and inertio-gravity (IG) waves (Kikuchi and Wang 2010). These super cloud clusters are also embedded with mesoscale convective systems (MCSs) or individual cloud clusters, which onset and decay within a time scale of hours.

As one of the essential features of the MJO, substantial mechanisms have been proposed to explain its eastward propagation, including the boundary layer frictional moisture convergence of wave-Conditional Instability of the Second Kind (CISK) theory (Chang and Lim 1988; Wang 1988; Wang and Li 1994; Wang and Chen 2017), wind-evaporation feedback in the theory of wind-induced surface heat exchange (WISHE) (Emanuel 1987; Neelin et al. 1987), and transport of mean moisture by MJO flows when MJO is regarded as a "moist mode" (Sobel and Maloney 2012, 2013; Wang et al. 2017). In these theories, the interactions between the MJO and other time-scale modes, which may be critical to the MJO dynamics according to its observed hierarchical structure, however, are not taken into consideration. With the moist static energy (MSE) budget diagnosis, Maloney (2009) suggests that the activities of the synoptic eddies are of great importance to the recharge and discharge of the intraseasonal MSE in the model, which favor the eastward propagation of the MJO. A "skeleton model" was proposed by adding the synoptic wave activities and low-level moisture advection to the Matsuno–Gill model (Majda and Stechmann 2009). Such a skeleton model successfully produces a non-dispersive, slowly eastward propagating mode with quadrupole vortex structure (Majda and Stechmann 2009). Another theory managed to connect the activities of the synoptic waves to the MJO variation is through parameterizing the eddy momentum and heating transport in the governing equations (Wang and Liu 2011; Liu and Wang 2012, 2013). In this theory, the eastward propagation of the MJO is stemming from the boundary layer frictional convergence, while the interaction of the MJO with eddies adjusts the phase speed, so that it can be closer to the observation. In addition to the models, some observational evidence also verifies that nonlinear modulations by the high-frequency waves (HFW) promote the eastward propagation of the MJO (Zhou and Li 2010; Hsu and Li 2011; Hsu et al 2011; Krishnamurti et al. 2016).

Although tremendous efforts have been devoted and diverse theories have been proposed, the multi-model intercomparison projects show that the deficiencies in simulating the intensity and eastward propagation of the MJO are non-negligible in the state-of-art models, especially over the MC region (Lin et al. 2006; Kim et al. 2009; Hung et al. 2013; Wang et al. 2017). Lin et al. (2008) suggested that the interaction of convective coupled equatorial waves associated with the MJO is of great importance to the MJO simulation. In this work, we will diagnose the effects of the two-way interactions between the HFW and MJO with the model results from the MJO Task Force (MJOTF) and the CEWEX Atmospheric System Studies (GASS) Panel. According to their performance in simulating the MJO eastward propagation over the MC region, the models are divided into good and poor model groups. The goal of this study is to figure out whether the two-way interaction between the HFW and MJO is critical to the MJO eastward propagation in the models, and what are the mechanisms that lead to the differences of the two-way interactions between good and poor model groups. The details of the data and methods are described in Sect. 2. The comparison of the MJO structure and the modulation of HFW by the MJO between the good and poor model group are analyzed in Sect. 3. The two types of upscale feedbacks from HFW to the MJO are discussed in Sect. 4. Section 5 gives a brief summary and discussion.

2 Data and methods

The data analyzed in this study is the 20-year climate simulations from the MJOTF/GASS MJO global model comparison project (Jiang et al. 2015; Wang et al. 2017; Wang and Lee 2017) (https://www.earthsystemcog.org/projects/gass-yotc-mip/). The purposes of this project are to understand, compare and estimate the heating, moistening and momentum transporting processes of the MJO in the climate models. All the variables are provided four times daily from 1991 to 2010 with global coverage in a $2.5° \times 2.5°$ resolution and they are averaged to daily data. The variables used for analysis include the three-dimensional zonal and meridional winds (u and v), pressure vertical velocity (ω), geopotential height (ϕ) and specific humidity (q) and the two-dimensional precipitation. The $1° \times 1°$ daily precipitation from Global Precipitation Climatology Project (GPCP, Huffman et al. 2001), and the $2.5° \times 2.5°$ three-dimensional atmospheric fields from the ERA-Interim reanalysis provided by the European Centre of Medium-Range Weather Forecasts (ECMWF) (Dee et al. 2011) are utilized to describe the observational MJO features and to compare with the model results. The GPCP and ERA-Interim datasets cover the period of 1997–2010. As we merely focus on the eastward propagation of MJO, only the boreal winter (Nov–Apr) is selected for analysis.

A temporal decomposition is applied to all of the variables. Firstly, the annual cycle is removed from the data. Then a given variable A is separated into three components with different time-scales by the Lanczos bandpass filter (Duchon 1979), including the high-frequency component (A', < 20 days), the MJO component ($\tilde{A}$, 20–100 days) and the low-frequency background state component ($\bar{A}$,

> 100 days). The MJO active (suppressed) events are identified when the intraseasonal filtered precipitation anomaly averaged over 5°–15° S, 125°–135° E (denoted by the blue boxes in Fig. 2) is larger (smaller) than one positive (negative) stand deviation. Similar features of the MJO structures and upscale feedbacks of the HFW are found in the composite results of active and suppressed MJO events, but with opposite signs. In this case, the composite difference between the active and suppressed events is analyzed in this study. In order to highlight the structure difference between the good and poor model group rather than the amplitude difference, all the fields in the models are normalized by dividing the corresponding precipitation anomaly of MJO averaged over 5°–15° S, 125°–135° E (amplitude of the MJO precipitation in each model shown in Table 1), then multiplying by a value of 3 mm day^{-1}.

3 Structures of the MJO and modulation of HFW by the MJO

By comparing the precipitation and zonal wind anomalies associated with the eastward-propagating MJO over the MC region in each model with the observations (figure not shown), six models (CNRM_CM, ECHAM5_SIT, MRI-AGCM, SPCAM3_AMIP, SPCCSM, TAMU_CAM4) are classified into the good model group, and another six models (CanCM4, CFSv2AMIP, CAM5ZMMicroCAPT, ISUGCM, MIROC5, MPI-ESM) are classified into the poor model group. The information of the 12 selected models is given in Table 1. Figure 1a presents the time evolution of 5°–15° S averaged MJO precipitation and zonal wind anomaly of the observation. Same as in observation, both MJO convection and flows of good model ensemble exhibit continuously eastward propagation (Fig. 1b), while significant westward propagating appears in the poor model group (Fig. 1c). Figure 2 displays the horizontal pattern of the MJO-scale precipitation and 850-hPa zonal wind. The extent of positive precipitation anomaly in the poor model group is smaller than the observation and the good model group.

When exploring the relationship between MJO and HFW with observational data, we have found that two MJO variables (zonal wind shear anomaly and specific humidity anomaly) are related to HFW variation (Zhu et al. 2019). The vertical structures of zonal wind shear anomaly and specific humidity anomaly are presented in Figs. 3 and 4. In the observation good model group, there is easterly wind shear of MJO over and in the west of the MJO convection and westerly wind shear in the east of the MJO convection. Although the vertical wind shear also exists in the poor model group, the intensity is weaker and it is more confined near the 120° E (Fig. 3). For the specific humidity anomaly, the intensity in the poor model group is also considerably smaller than the observation and good model group (Fig. 4). Besides, the boundary layer leading of the intraseasonal filtered specific humidity is more apparent in the observation and good model group than in the poor model group.

The spatial variation of the stand deviation of vorticity anomalies indicates the modulation of the background MJO to the HFW activities. In observation (Fig. 5a), the enhanced specific humidity anomaly and easterly wind shear anomaly induce the strengthened HFW variation over and to the west of MJO convection. Correspondingly, the westerly wind shear anomaly causes the weakened HFW variation to the east of

Table 1 Information of good model group and poor model group

	Institute	Model name	Precipitation amplitude (mm/day)
(a) Good models			
1	Centre National de la Recherche Scientifique/Météo-France	CNRM-CM	11.05
2	Academia Sinica	ECHAM5-SIT	11.10
3	Meteorological Research Institute, Japan	MRI-AGCM	10.71
4	Colorado State University	SPCAM3_AMIP	13.52
5	George Mason University	SPCCSM	13.36
6	Texas A&M University	TAMU_CAM4	11.63
(b) Poor models			
1	Canadian Centre for Climate Modelling and Analysis	CanCM4	5.68
2	Climate Prediction Center, NOAA/NCEP	CFSv2AMIP	10.14
3	Lawrence Livermore National Laboratory	CAM5ZMMicroCAPT	8.28
4	Iowa State University	ISUGCM	8.98
5	Atmosphere and Ocean Research Institute/National Institute for Environmental Studies/JAMSTEC, Japan	MIROC5	12.81
6	Max Planck Institute for Meteorology	MPI-ESM	11.24

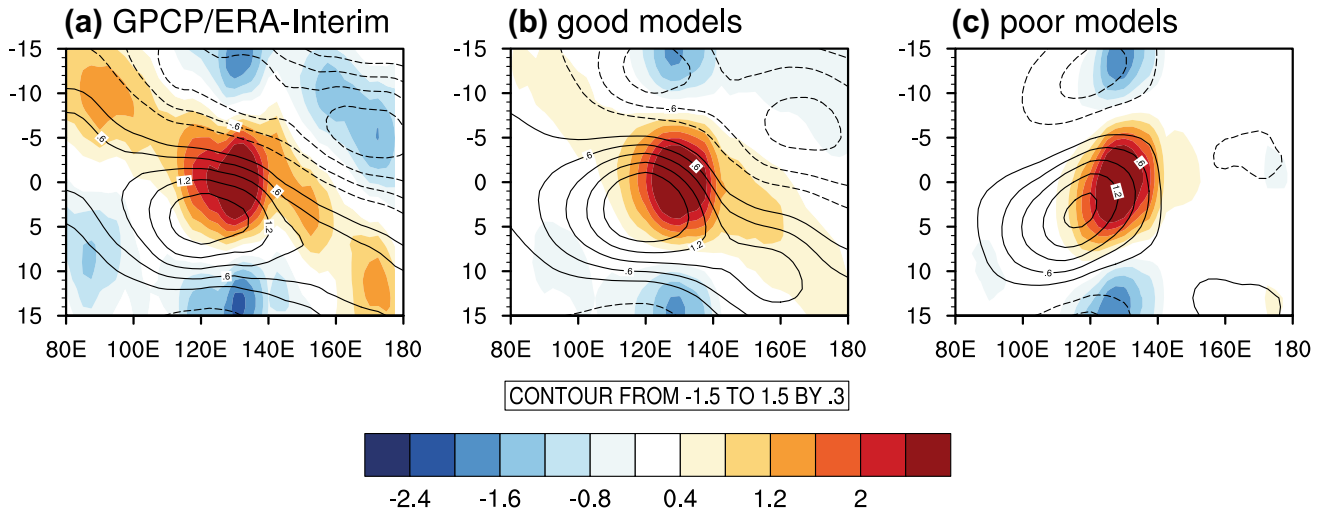

Fig. 1 The Time-longitude cross-section of 5°–15° S averaged intraseasonal filtered (shading, unit: mm day^{-1}) and zonal wind at 850-hPa (contour, unit: ms^{-1}) for MJO active phase minus suppressed phase of GPCP and ERA-Interim. **b**, **c** As in **a**, but for good model group and poor model group

MJO convection. The response of the HFW variation to the MJO wind field is consistent with the previous studies about modulation of HFW from the MJO (Wang and Xie 1996; Maloney and Dickinson 2003; Maloney 2009). The intensity variation of HFW is slightly weaker in the good model group than observation, but most of variation passed the significance test (Fig. 5b). In the poor model group, the increased intensity of HFW is constrained over the MJO convection center and there is no significant decreased intensity to the east of convection center (Fig. 5c). As we mentioned above, the distinction between the good and poor model group is attributed to the more constricted, weaker MJO specific humidity and zonal wind shear anomaly in the poor model group.

4 Feedback from HFW to the MJO

4.1 Feedback from nonlinear rectification of condensational heating anomalies of HFW

The apparent moisture sink (Q_2) is first introduced by Yanai et al. (1973) and it can be retrieved from the specific humidity tendency, the horizontal and the vertical specific humidity advection. The intraseasonal apparent moisture sink anomaly is given as:

$$\tilde{Q}_2 = -L\widetilde{\frac{\partial q}{\partial t}} - L\left(\widetilde{V\cdot\nabla q}\right) - L\left(\widetilde{\omega\frac{\partial q}{\partial p}}\right) \tag{1}$$

where the tilde represents projecting the variables into the MJO time scale, L is the latent heat of condensation, q is the specific humidity, t is the time, V is the horizontal wind vector, ∇ is the horizontal gradient operator, ω is the vertical pressure velocity, p denotes the pressure, and Q_2 represents the latent heating attributing to condensation, evaporation and subgrid-scale moisture flux convergence. The $\tilde{Q}_2$ is dominated by the latent heating due to condensation, and therefore it can represent the condensational heating of MJO.

The upscale feedback from the HFW to the Q_2 or the nonlinearly rectified apparent moisture sink is obtained through the interaction between the high-frequency component and other time-scale components. There are two diagnostics to obtain the intraseasonal nonlinearly rectified $\tilde{Q}_2$:

$$\widetilde{Q_{2\_LH}} = -L(u'+\bar{u})\widetilde{\frac{\partial(q'+\bar{q})}{\partial x}} - L(v'+\bar{v})\widetilde{\frac{\partial(q'+\bar{q})}{\partial y}} - L(\omega'+\bar{\omega})\widetilde{\frac{\partial(q'+\bar{q})}{\partial p}} \tag{2}$$

$$\widetilde{Q_{2\_T-Li}} = \widetilde{Q_2} - \left[-L(\tilde{u}+\bar{u})\widetilde{\frac{\partial(\tilde{q}+\bar{q})}{\partial x}} - L(\tilde{v}+\bar{v})\widetilde{\frac{\partial(\tilde{q}+\bar{q})}{\partial y}} - L(\tilde{\omega}+\bar{\omega})\widetilde{\frac{\partial(\tilde{q}+\bar{q})}{\partial p}}\right] \tag{3}$$

where the Q_{2_LH} represents the condensational heating contributed by the rectification of the high-frequency component with the low-frequency background state component, the Q_{2_T-LI} represents the condensational heating contributed by the rectification of the high-frequency component with both the MJO component and the low-frequency background state component. All of the superscripts in the

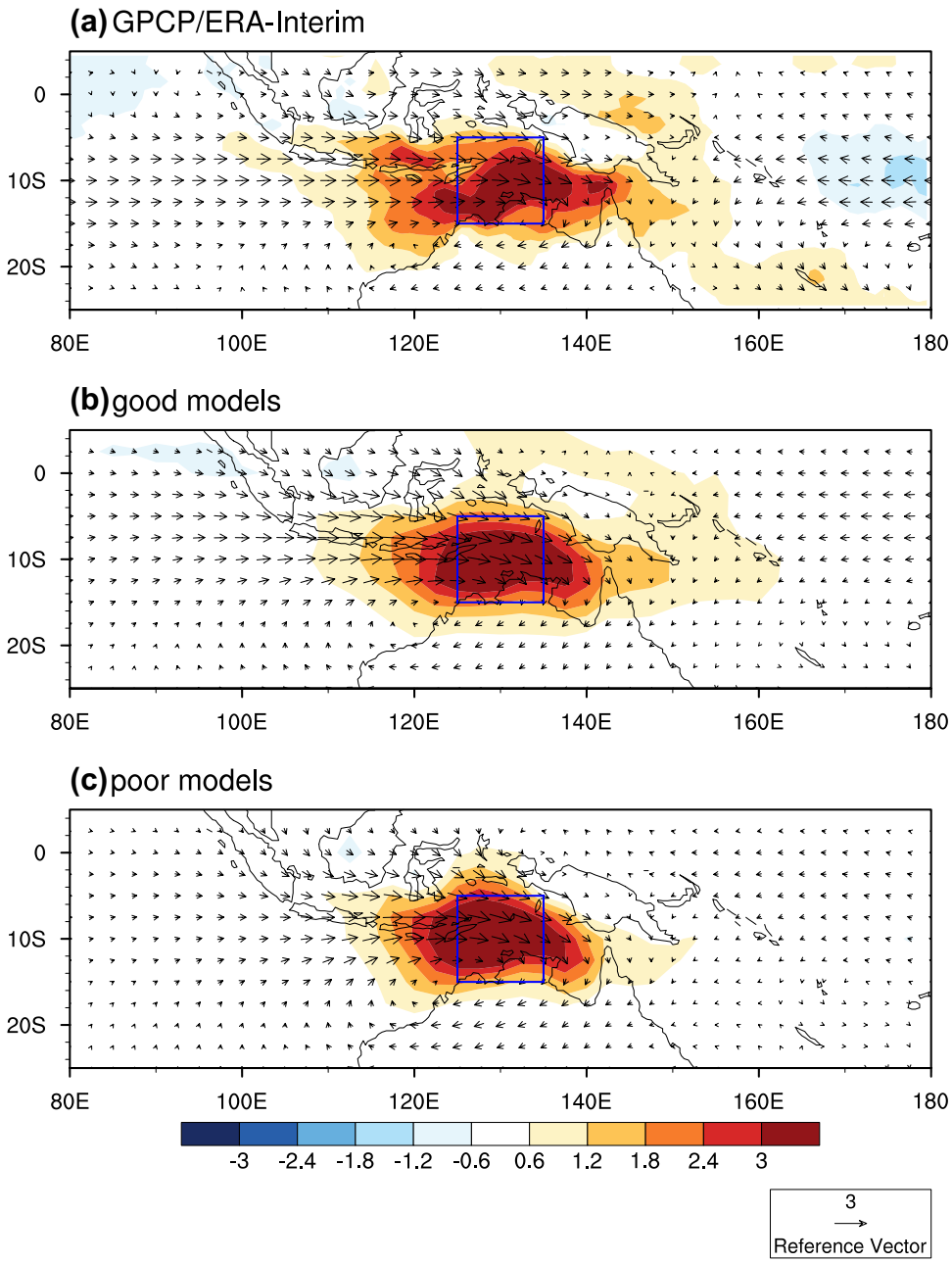

Fig. 2 **a** The horizontal structure of the intraseasonal filtered precipitation (shading, unit: mm day^{-1}) and wind at 850-hPa (vector, unit: ms^{-1}) for MJO active phase minus MJO suppressed phase of GPCP and ERA-Interim data. The blue box indicates the 15° S–5° S, 125°–135° E. **b**, **c** As in **a**, but for good model group and poor model group

equations are introduced in Sect. 2, and a more detail introduction of Eqs. (3) and (4) is described in Hsu and Li (2011) and Zhu et al. (2019).

Figure 6 (top) illustrates the time evolution of the regionally averaged $\tilde{Q}_2$ in the east of the MJO convection. As shown in the observation and the good model group, the positive condensational heating anomaly in the east of MJO convection first appears in the boundary layer before day 0 (Day 0 is the day when maximum MJO convection established at the 130° E) and it gradually deepens to the middle and upper troposphere in subsequent days. The boundary layer vertical integration of the east and west boxes averaged $\tilde{Q}_2$ are displayed to compare the different time evolution of $\tilde{Q}_2$ between the east and west of MJO convection [Fig. 6 (bottom)]. In the observation and good model group, $\tilde{Q}_2$ over the west box decreases after day-6 while the $\tilde{Q}_2$ over the east box gradually grows, and finally $\tilde{Q}_2$ in the east box excesses the west box. The explanation of how is the evolution of $\tilde{Q}_2$ in the east and west of MJO convection supporting the eastward propagation of MJO convection given in the following. In the east of the MJO convection, there is developing of the shallow condensational heating. It creates an unstable environment and favors the continuous moisture convergence, which further generates the condensational heating of the congest

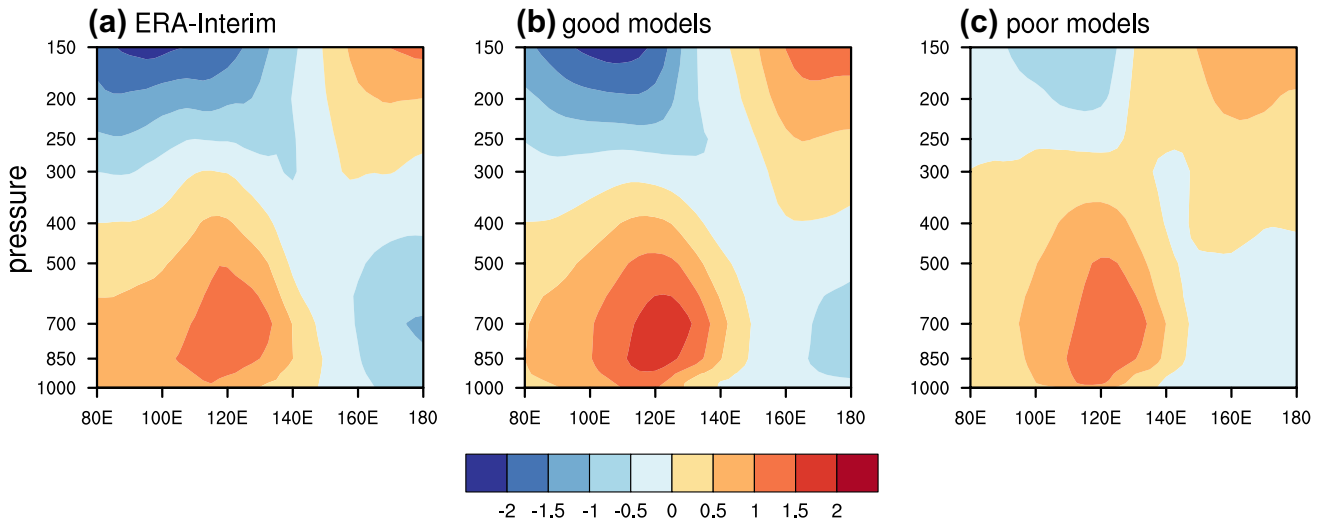

Fig. 3 **a** The pressure-longitude cross-section of 5°–15° S averaged intraseasonal filtered zonal wind (unit: ms^{-1}) for MJO active phase minus suppressed phase of ERA-interim data. **b**, **c** As in **a**, but for good model group and poor model group

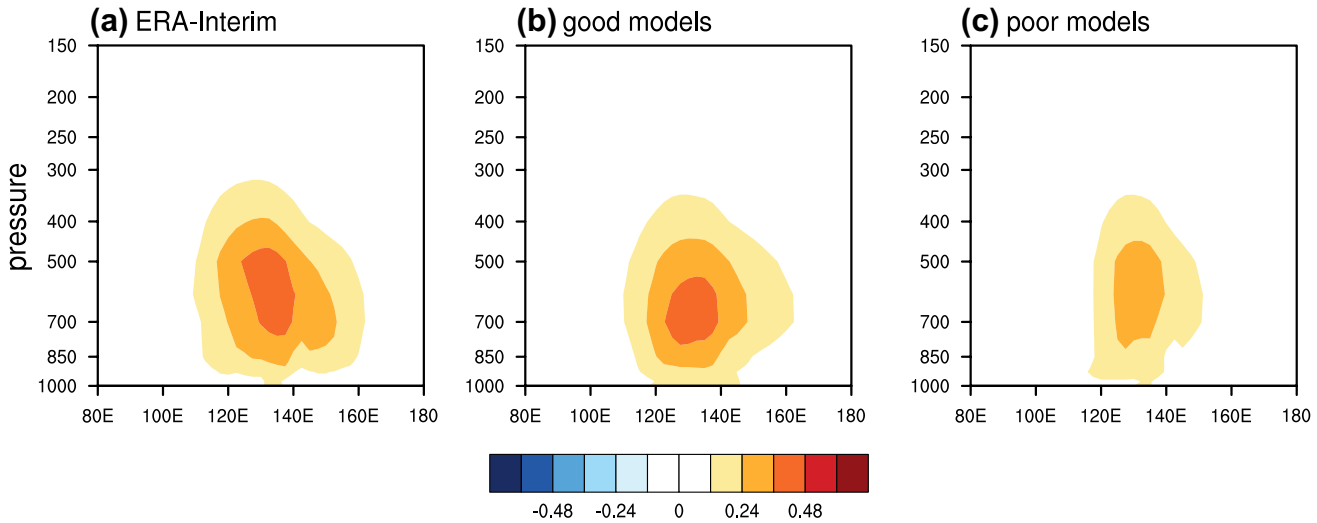

Fig. 4 **a** The pressure-longitude cross-section of 5°–15° S averaged intraseasonal filtered specific humidity (unit: g/kg) for MJO active phase minus suppressed phase of ERA-interim data. **b**, **c** As in **a**, but for good model group and poor model group

clouds and the new deep convection. Meanwhile, the intraseasonal condensational heating decays over the west of the MJO convection. The establishment of the new deep convection in the east of MJO convection and the decay of it in the west favors the eastward propagation of the MJO convection. A similar mechanism about the importance of the onset of shallow convection to MJO deep convection is also discussed in Benedict and Randall (2007) and Hsu and Li (2012). Although the amplitude of $\tilde{Q}_2$ in the east of MJO convection exhibits the slowly growing feature in the poor model group as well (Fig. 6c (top)), it is consistently smaller than $\tilde{Q}_2$ in the west [Fig. 6c (bottom)]. Therefore, no eastward propagation of the MJO convection in the poor model group.

Why the condensational heating anomaly in the east of MJO convection can excess its counterpart in the west in the observation and the good model group but it cannot in the poor model group and how does the nonlinear rectification of the HFW contribute to this difference? To address the problem, the vertical structures of $\tilde{Q}_2$ are presented in Fig. 7. Because the time for the intraseasonal condensational heating growing from shallow to deep is about 5-days, each model is averaged of 5-days before the MJO deep convection appearing and then composite in the good and the poor

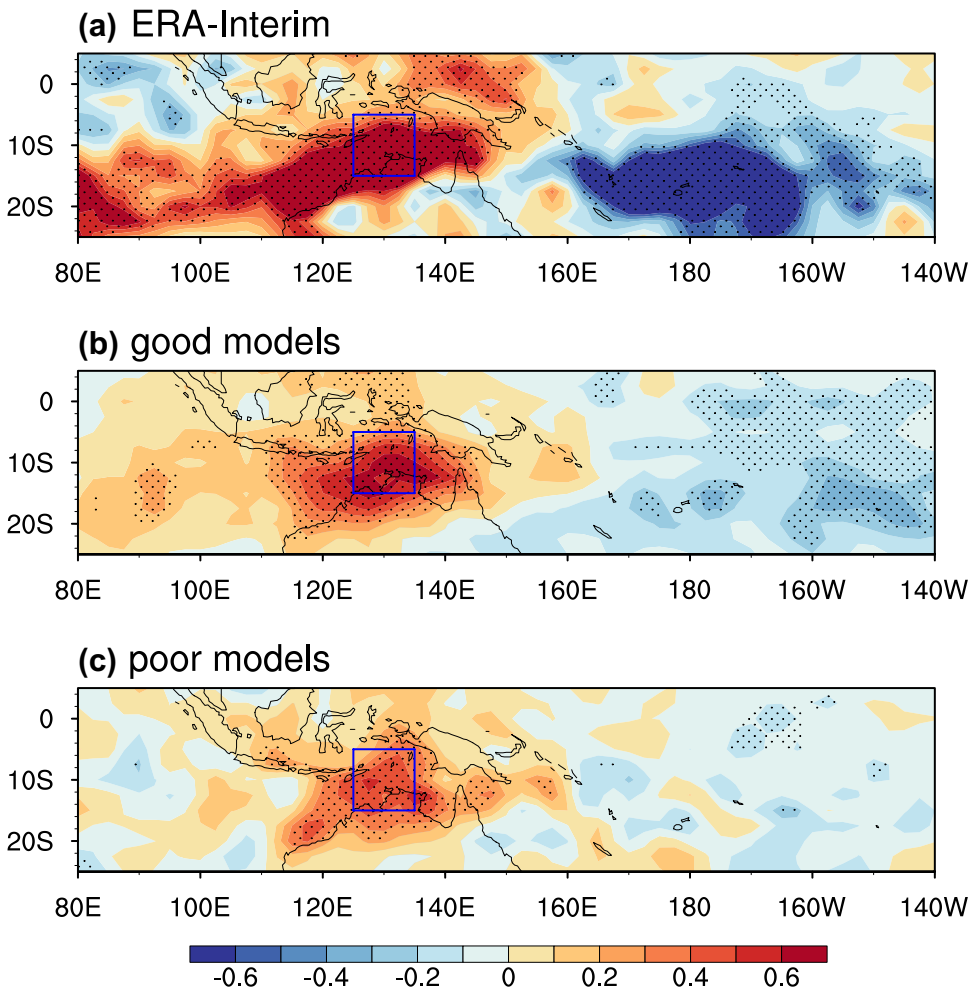

Fig. 5 **a** Composited difference of standard deviation of 20-day high-pass filtered vorticity at 850-hPa (unit: 10^{-6} s^{-1}) between MJO active phase and suppressed phase of ERA-Interim data. Dot areas are difference significant at 95% level. The blue box indicates the 15° S–5° S, 125°–135° E. **b**, **c** As in **a**, but for good model group and poor model group

model group separately. Same as illustrated in Fig. 6 (top), in the east of MJO convection, there is shallow condensational heating anomaly developing in the observation and the good model group (Fig. 7a, b). However, no clear development occurs in the poor model group (Fig. 7c). The vertical structure of $\widetilde{Q_{2\_T-LI}}$ is presented to explore the effect of nonlinear rectification of HFW on the development of the shallow condensational heating anomaly (Fig. 8). The structure of $\widetilde{Q_{2\_LH}}$ is similar to $\widetilde{Q_{2\_T-LI}}$, but with smaller amplitude (figures not shown). In the observation and the good model group, there is positive (negative) $\widetilde{Q_{2\_T-LI}}$ appearing in the boundary layer in the east (west) of the MJO convection (Fig. 8a, b). The positive $\widetilde{Q_{2\_T-LI}}$ is in the same location as the shallow condensational heating of MJO and therefore feeds back to its development. To quantify the contribution from nonlinearly rectified condensational heating to the MJO shallow convective heating, the boundary layer (1000–700-hPa) averaged $\widetilde{Q_{2\_LH}}$ and $\widetilde{Q_{2\_T-LI}}$ to $\tilde{Q}_2$ in the east of MJO convection are calculated, which are 10–40% and 20–70% respectively (Fig. 9). Besides, the negative $\widetilde{Q_{2\_T-LI}}$ in the west of the MJO convection in the observation and the good model group suggests that the nonlinear rectification of the HFW also favors the decaying of the original MJO convection. Different from the observation and the good model group, there is no apparent asymmetric $\widetilde{Q_{2\_T-LI}}$ in the boundary layer in the poor model group, which demonstrates that the nonlinear rectification of the HFW does not favors the eastward propagation of the MJO convection in the poor model group.

To illustrate the mechanism for the distinct $\widetilde{Q_{2\_T-LI}}$ and $\widetilde{Q_{2\_LH}}$ in the good and poor group, we analyzed every component in the $\widetilde{Q_{2\_LH}}$ and $\widetilde{Q_{2\_T-LI}}$ separately and discovered the difference is stemmed from the meridional advection of specific humidity anomaly ($-Lv'\frac{\partial q'}{\partial y}$) (Fig. 10a). $\widetilde{-Lv'\frac{\partial q'}{\partial y}}$ is the dominant component within the $\widetilde{Q_{2\_LH}}$ and $\widetilde{Q_{2\_T-LI}}$. In the observation and the good model group, without disturbances from the irrelevant terms, $\widetilde{-Lv'\frac{\partial q'}{\partial y}}$ shows a more conspicuous asymmetric feature in the east and west of the MJO convection than $\widetilde{Q_{2\_LH}}$ and $\widetilde{Q_{2\_T-LI}}$. The positive (negative) $\widetilde{-Lv'\frac{\partial q'}{\partial y}}$ in the east (west) of MJO convection extends from boundary layer to middle troposphere (Fig. 10 a, b), which suggests it helps the development of

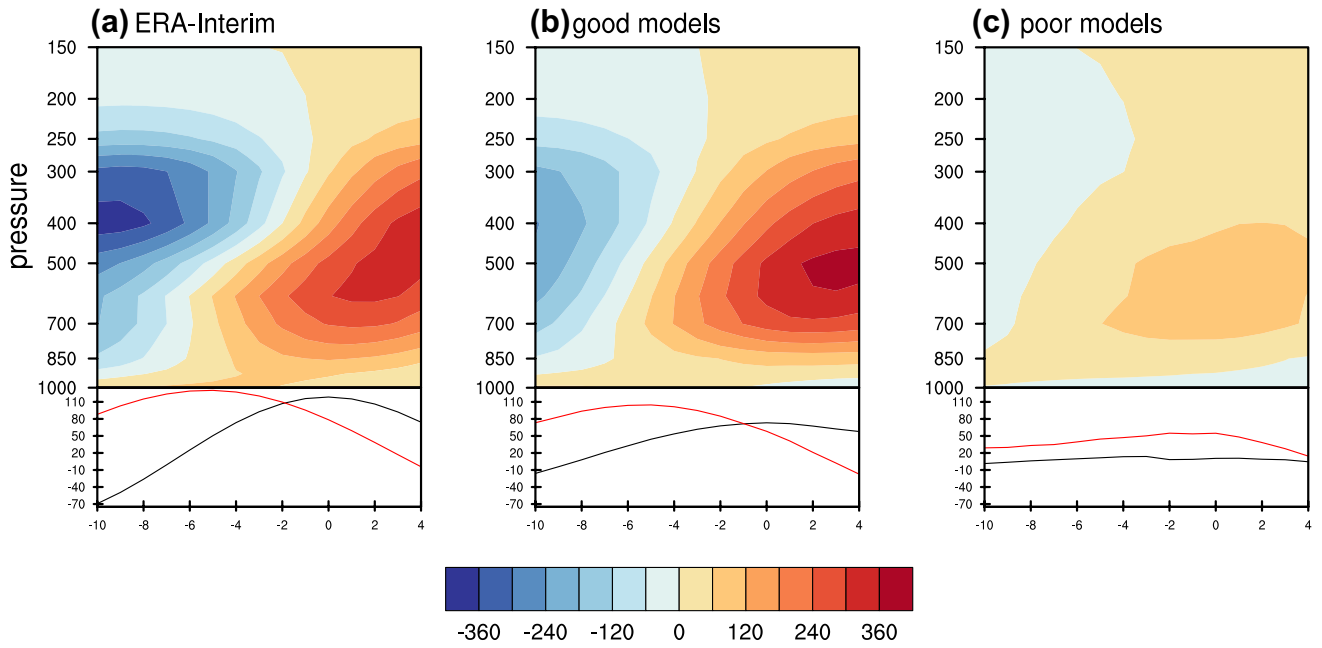

Fig. 6 **a** (top) The pressure-time cross-section of 5°–15° S, 140°–180° E averaged $\tilde{Q}_2$ (unit: W m^{-2}) from day-8 to day 4 for MJO active phase minus suppressed phase of ERA-Interim data, (bottom) the boundary layer (1000–700-hPa) vertical integration of the 5°–15° S, 140° E–180° averaged $\tilde{Q}_2$ (black line) and boundary layer vertical integration of the 5°–15° S, 85°–125° E averaged $\tilde{Q}_2$ (red line) for MJO active phase minus suppressed phase of ERA-Interim data. **b**, **c** As in **a**, but for good model group and poor model group

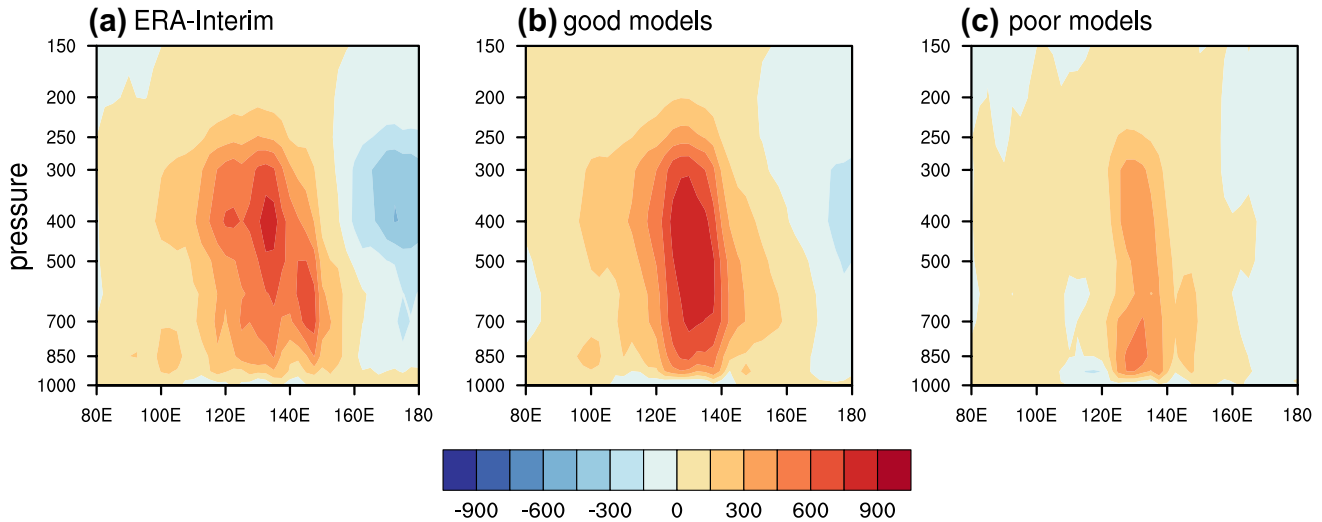

Fig. 7 **a** The pressure-longitude cross-section of 5°–15° S averaged $\tilde{Q}_2$ (unit: W m^{-2}) for 5-days before MJO deep convection happening averaging for MJO active phase minus suppressed phase of ERA-Interim data. **b**, **c** As in **a**, but for good model group and poor model group

the condensational heating of the shallow and the congestus clouds. There is no apparent asymmetric feature of $-\widetilde{Lv'\frac{\partial q'}{\partial y}}$ in the poor model group (Fig. 10c), so no asymmetric $\widetilde{Q_{2\_LH}}$ and $\widetilde{Q_{2\_T-LI}}$ appears as well. The explanation of the upscale feedback from the meridional wind anomaly and moisture anomaly of the HFW to the MJO convection is associated with the modulation of MJO to HFW shown in Fig. 5. The weakened (strengthened) activity of the HFW accompanying with decreased (increased) meridional wind anomaly (v') and specific humidity anomaly (q') inhibits (enhances) the negative meridional moisture advection in the east (west) of MJO convection, which means that the mixing of the dry air from extratropic to

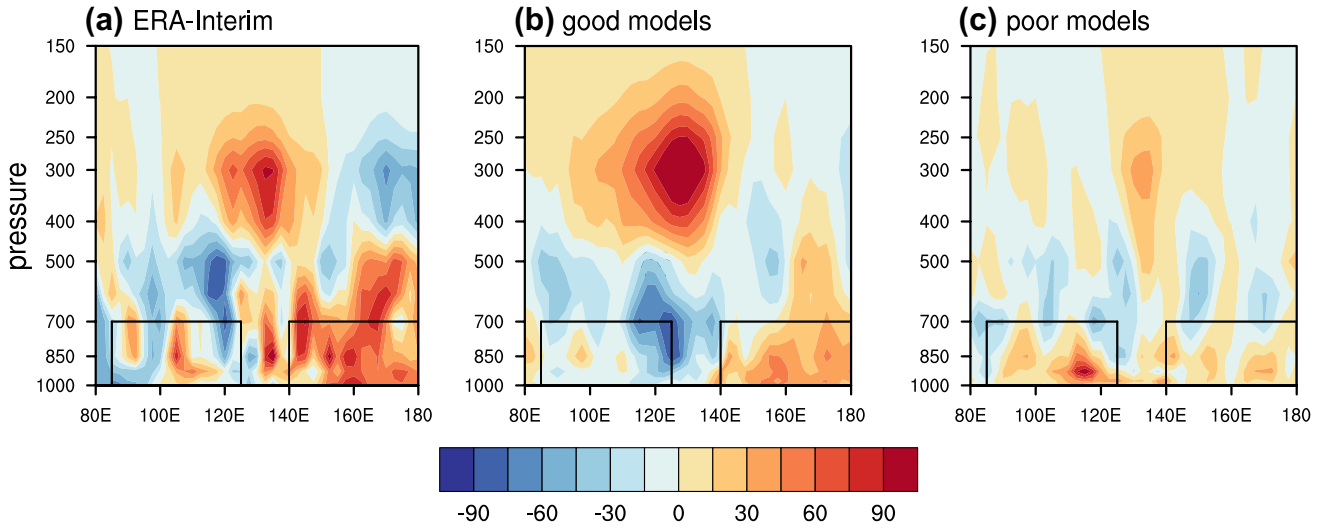

Fig. 8 **a** The pressure-longitude cross-section of 5°–15° S averaged $\widetilde{Q_{2\_T-LI}}$ (unit: W m^{-2}) for 5-days before MJO deep convection happening averaging for MJO active phase minus suppressed phase of ERA-Interim data. The black boxes indicate the 85°–125° E and 140° E–180° for boundary layer (1000~700-hPa). **b**, **c** As in **a**, but for good model group and poor model group

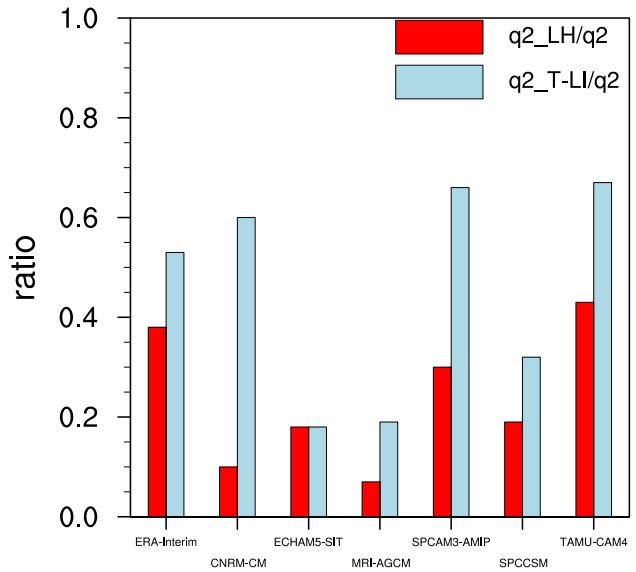

Fig. 9 Ratio of boundary layer vertical integration of 5°–15° S, 140°–180° E averaging of 5-days before MJO deep convection happening averaged $\widetilde{Q_{2\_T-LI}}$ and $\widetilde{Q_{2\_LH}}$ to $\tilde{Q}_2$ for MJO active phase minus MJO suppressed phase of ERA-Interim data and good models (red bar is for $\widetilde{Q_{2\_LH}}$ and blue bar is for $\widetilde{Q_{2\_T-LI}}$.)

tropic region is decreased (increased). As a consequence, there is positive (negative) $-\widetilde{Lv'\frac{\partial q'}{\partial y}}$ in the east (west) of the MJO convection in the observation and the good model group. The schematic figure about the upscale feedback from the nonlinear rectification of condensational heating to the MJO is shown in Zhu et al. (2009). Maloney (2009) suggested a similar effect of meridional advection from the synoptic eddy on recharging and discharging the moist static energy of the MJO. However, in the poor model group, the decrease (increase) of HFW intensity is not significant in the east (west) of MJO convection. Thus, no corresponding asymmetric $-\widetilde{Lv'\frac{\partial q'}{\partial y}}$ is shown in the poor model group.

4.2 Feedback from eddy momentum transport of HFW

Figure 11 displays the vertical structures of the MJO zonal wind anomaly ($\tilde{u}$) and zonal wind tendency anomaly ($\frac{\partial \tilde{u}}{\partial t}$). In the observation and good model group, a positive (negative) $\frac{\partial \tilde{u}}{\partial t}$ extends from the center of $\tilde{u}$ to the transitional region (the region that $\tilde{u}$ changes from positive anomaly to negative anomaly) in the lower (upper) troposphere. $\frac{\partial u}{\partial t}$ in the center of $\tilde{u}$ works to modulate the intensity of $\tilde{u}$, and $\frac{\partial u}{\partial t}$ in the transitional region demonstrates the propagating tendency of $\tilde{u}$. In the observation and good model group, with positive (negative) $\frac{\partial \tilde{u}}{\partial t}$ in the transitional region in the lower (upper) troposphere, $\tilde{u}$ will increase (decrease) in this region in the next moment, which displays as eastward propagation of $\tilde{u}$. However, $\frac{\partial u}{\partial t}$ in the poor model group is mainly constricted near the center of the MJO zonal wind and almost zero in the transitional region. Hence, $\tilde{u}$ does not show the eastward propagation in the poor model group. From analyzing the MJO zonal momentum equation, we want to elucidate the reason for different intraseasonal zonal wind tendencies in the transitional region between the good and poor model group. The MJO zonal momentum equation is expressed as:

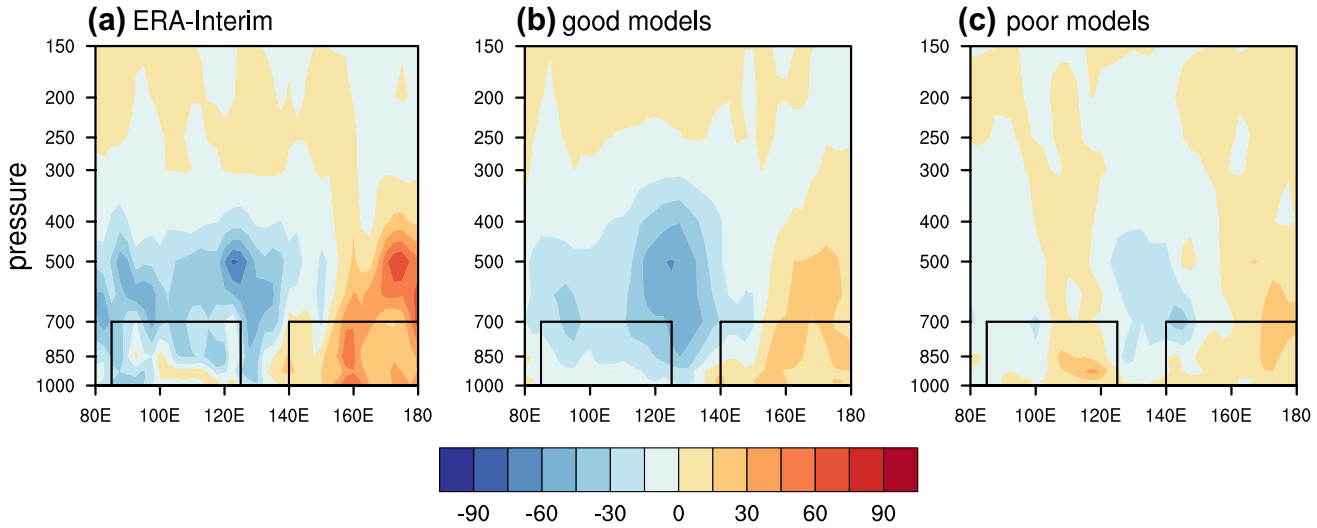

Fig. 10 **a** The pressure-longitude cross-section of 5°–15° S averaged $-\widetilde{Lv'\frac{\partial q'}{\partial y}}$ (unit: W m^{-2}) for 5-days before MJO deep convection happening averaging for MJO active phase minus suppressed phase of ERA-Interim data. The black boxes indicate the 85°–125° E and 140° E–180° for boundary layer (1000~700-hPa). **b**, **c** As in **a**, but for good model group and poor model group

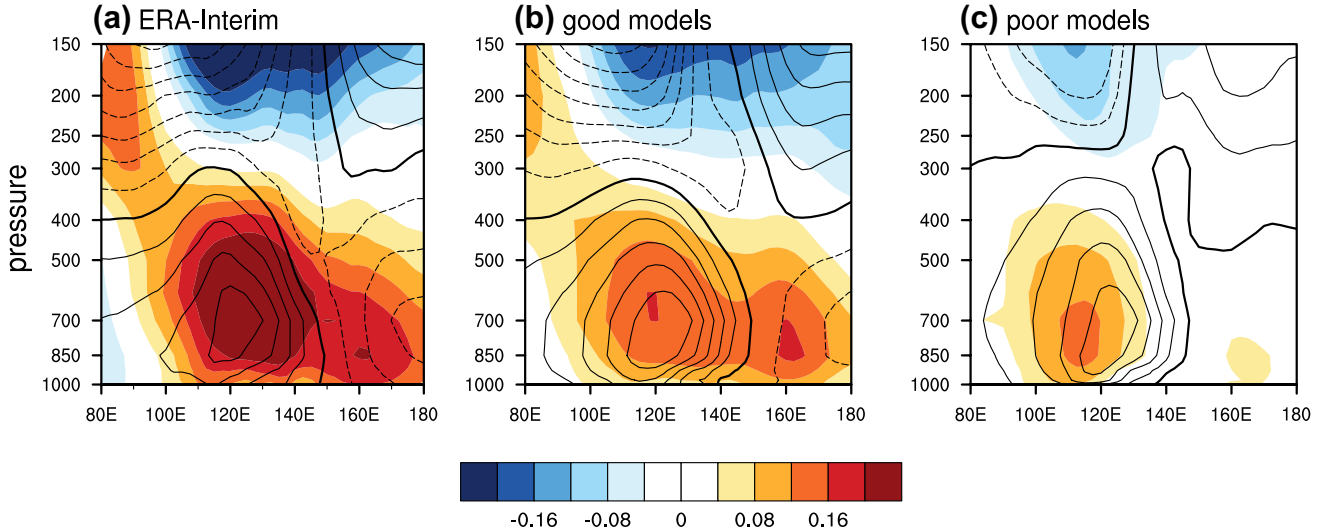

Fig. 11 **a** The pressure-longitude cross-section of 5°–15° S averaged $\widetilde{\tilde{u}}$ (contour, unit: ms^{-1}. thick line is zero, interval is 0.3 ms^{-1}) and $\widetilde{\frac{\partial u}{\partial t}}$ (shading, unit: 10^{-5} s^{-1}) for MJO active phase minus suppressed phase of ERA-Interim data. **b**, **c** As in **a**, but for good model group and poor model group

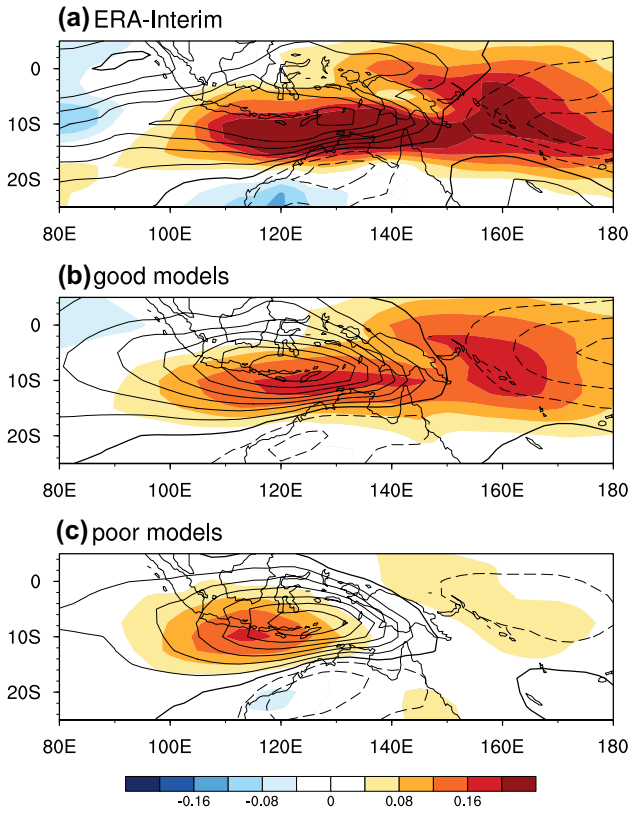

Fig. 12 **a** The horizontal structure of $\tilde{u}$ (contour, unit: ms^{-1}, black thick line is zero and interval is 0.3 ms^{-1}) and $\frac{\partial \tilde{u}}{\partial t}$ (shading, unit: 10^{-5} s^{-1}) at 850-hPa for MJO active phase minus suppressed phase of ERA-Interim data. **b**, **c** As in **a**, but for good model group and poor model group

$$\begin{aligned}\widetilde{\frac{\partial u}{\partial t}} = & \underbrace{\left(-\frac{\widetilde{\partial u'u'}}{\partial x}-\frac{\widetilde{\partial u'v'}}{\partial y}-\frac{\widetilde{\partial u'\omega'}}{\partial p}\right)}_{termA1} \\ & + \underbrace{\left(-u'\frac{\widetilde{\partial(\tilde{u}+\bar{u})}}{\partial x}-v'\frac{\widetilde{\partial(\tilde{u}+\bar{u})}}{\partial y}-\omega'\frac{\widetilde{\partial(\tilde{u}+\bar{u})}}{\partial p}\right)}_{termA2} \\ & + \underbrace{\left(-(\tilde{u}+\bar{u})\frac{\partial u'}{\partial x}-(\tilde{v}+\bar{v})\frac{\partial u'}{\partial y}-(\tilde{\omega}+\bar{\omega})\frac{\partial u'}{\partial p}\right)}_{termA3} \\ & + \underbrace{\left(-(\tilde{u}+\bar{u})\frac{\partial(\tilde{u}+\bar{u})}{\partial x}-(\tilde{v}+\bar{v})\frac{\partial(\tilde{u}+\bar{u})}{\partial y}-(\tilde{\omega}+\bar{\omega})\frac{\partial(\tilde{u}+\bar{u})}{\partial p}-\frac{\partial\tilde{\phi}}{\partial x}+f\tilde{v}\right)}_{termB}\end{aligned} \tag{4}$$

where t denotes the time, u and v are the zonal and meridional winds, p is the pressure, ϕ is the geopotential height, f is the Coriolis parameter. *TermA* is the HFW involved terms, including the eddy momentum flux divergence ($termA_1$), the advection of intraseasonal and low-frequency background state momentum by the HFW flow ($termA_2$) and the advection of high-frequency momentum by the low-frequency background state and the intraseasonal flows ($termA_3$). *TermB* consists of all of the no HFW involved terms. The sum of *termA* and *termB* cannot exactly balance the MJO zonal wind tendency because of lacking the subgrid-scale turbulent flux and the coarse resolution of data, but these two terms can still reflect the contribution from or not from the HFW to the MJO zonal wind tendency.

The largest contribution from the nonlinear rectification of HFW to $\widetilde{\frac{\partial u}{\partial t}}$ is at 850-hPa so that the following analysis will focus on this level. The horizontal pattern of $\widetilde{\frac{\partial u}{\partial t}}$ at 850-hPa shows a similar feature as in the pressure-longitude cross-section figure. $\widetilde{\frac{\partial u}{\partial t}}$ extends to the transitional region in the observation and good model group, and almost no positive $\widetilde{\frac{\partial u}{\partial t}}$ shows in the transitional region in the poor model group (Fig. 12). The transitional region averaged $\widetilde{\frac{\partial u}{\partial t}}$, $\widetilde{termA}$ and $\widetilde{termB}$ are shown in Fig. 13 to figure out why the $\widetilde{\frac{\partial u}{\partial t}}$ is different between the good and poor model group. It shows the contribution from $\widetilde{termA}$ to $\widetilde{\frac{\partial u}{\partial t}}$ is analogous in the good and poor models, while the contribution from $\widetilde{termB}$ is opposite in two groups. $\widetilde{termB}$ shows a positive anomaly in the observation and good models and a negative anomaly in the poor models. Thus, the offset of the $\widetilde{termA}$ and $\widetilde{termB}$ causes $\widetilde{\frac{\partial u}{\partial t}}$ approximate to zero in the transitional region in the poor models.

The analogous $\widetilde{termA}$ in the good and poor model group is related to the modulation of the MJO to the HFW intensity over the MJO convection region. The intraseasonal zonal eddy momentum flux divergence ($-\widetilde{\frac{\partial u'u'}{\partial x}}$) is the largest contributor among $\widetilde{termB}$. In Sect. 3, we discussed that the significant increase of the HFW intensity over the MJO

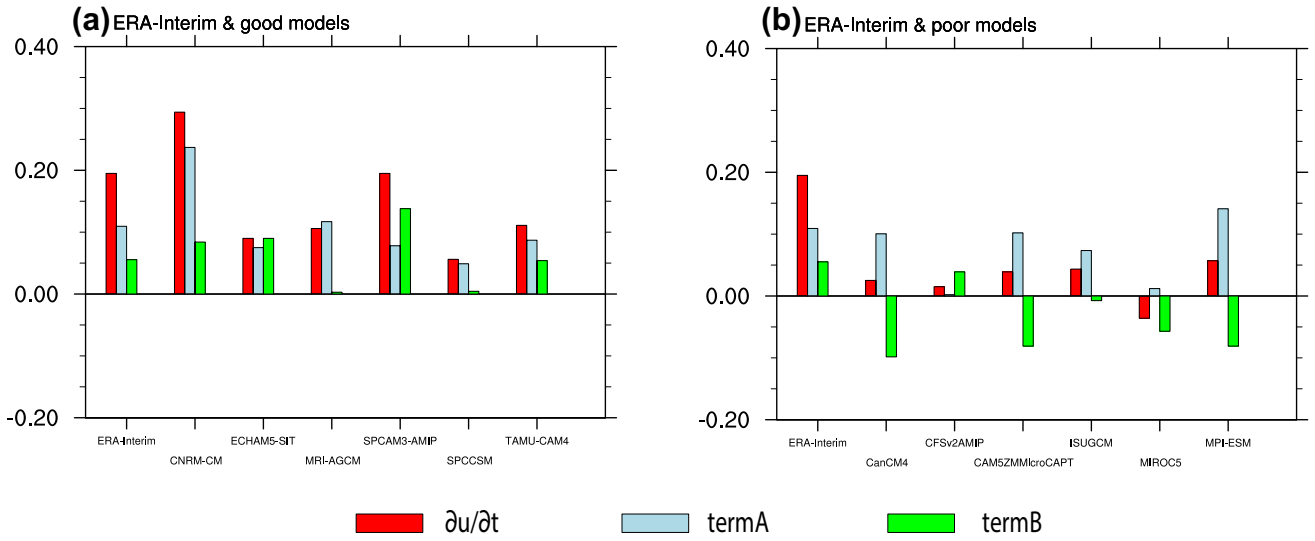

Fig. 13 **a** The $\widetilde{\frac{\partial u}{\partial t}}$ (red bars), $\widetilde{termA}$ (blue bars) and $\widetilde{termB}$ (green bars) averaged over the east zonal wind transitional region minus they averaged over the west zonal wind transitional region at 850-hPa of observation and good models (unit: 10^{-5} s^{-1}). **b** As in **a**, but for the observation and poor models. The MJO zonal wind transitional region is defined as a latitude 10°× longitude 20° box. The latitude for observation and models is 5°–15° S. The longitude are 135°–155° E for ERA-Interim data, 142.5°–162.5° E for CNRM-CM, 135°–155° E for ECHAM5-SIT, 140°–160° E for MRI-AGCM, 150°–170° E for SPCAM3-AMIP, 150°–170° E for SPCCSM, 140°–160° E for TAMU-CAM4, 130°–150° E for CanCM4, 142.5°–162.5° E for CFS-v2AMIP, 140°–160° E for CAM5ZMMicroCAPT, 130°–150° E for ISUGCM, 145°–165° E for MIROC5, 132.5°–152.5° E for MPI-ESM

convection region exists in both good and poor model group. The enhancement of the zonal wind of HFW (u') induces the positive intraseasonal zonal eddy momentum flux ($\widetilde{u'u'}$) over the MJO convection region (figure not shown). The divergence of $\widetilde{u'u'}$ primarily results in the positive $-\frac{\partial \widetilde{u'u'}}{\partial x}$ in the transitional region in both good and poor model group. The schematic diagram of upscale feedback from the eddy momentum transport to the MJO zonal wind is included in Zhu et al. (2019). The essential explanation for distinct propagation between the good and poor model groups is attributed to the contrary $\widetilde{termB}$. It found that the intraseasonal flows are weaker in the poor model group than the good model group, especially to the east of 140° E, which makes the components like $\frac{\partial \tilde{u}}{\partial x}$ and $\tilde{v}$ weaker in the poor model group (Fig. 14). Thus, the sum of three dominant positive anomalies ($f\tilde{v}$, $-\bar{u}\frac{\partial \tilde{u}}{\partial x}$ and $-\tilde{v}\frac{\partial \tilde{u}}{\partial y}$) among $\widetilde{termB}$ is smaller than the negative $-\frac{\partial \widetilde{\phi}}{\partial x}$, which results in the negative $\widetilde{termB}$ over the transitional region in the poor model group (Fig. 15).

5 Conclusion and discussion

The convection and flows of MJO can exert significant influences on the multiscale climate and weather phenomena. The interaction between the MJO and the HFW may be critical to the MJO dynamics based on the hierarchical structure of the MJO convective envelope. The effect of HFW on the eastward propagation of MJO has been verified with the observational data and some intermediate theoretical models. In this study, we want to explore the performance of the MJO eastward propagation, estimate the significance of two-way interaction between MJO and HFW to the MJO eastward propagation and investigate the mechanisms of two-way interaction with the model data from the 12 MJOTF/GASS models of 20-years period.

The good and poor model groups are determined through the performance of eastward propagation of the MJO precipitation and zonal wind anomaly. Two fields (zonal wind shear anomaly and specific humidity anomaly) of MJO are associated with the modulation to the HFW. The zonal wind shear anomaly is weaker and more limited near the MJO convection center in the poor model group compared to the observation and the good model group. The specific humidity anomaly is also weaker in the poor model group. The modulation of the HFW by the MJO is regionally dependent on the extent and intensity of zonal wind shear and specific humidity anomaly of the MJO. There is a significant increase (decrease) of HFW intensity over and to the west (east) of MJO convection in the observation and the good model group, while there is only enhanced HFW confined over the MJO convective center in the poor model group.

Two types of upscale feedback from the HFW to the MJO are investigated. The first upscale feedback diagnosed is the

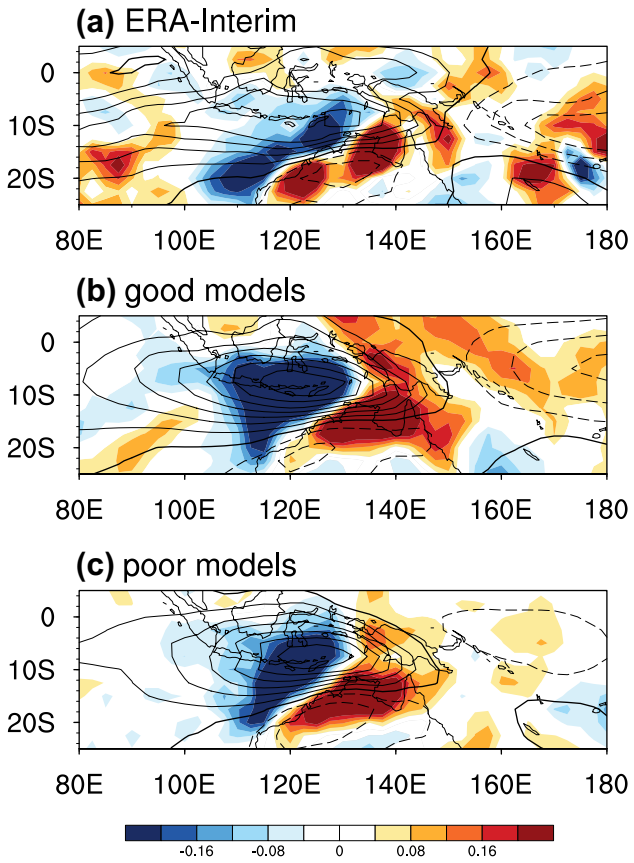

Fig. 14 **a** The horizontal structure of $\tilde{u}$ (contour, unit: ms^{-1}, black thick line is zero and interval is 0.3 ms^{-1}) and $\overline{termA}$ (shading, unit: 10^{-5} s^{-1}) at 850-hPa for MJO active phase minus suppressed phase of ERA-Interim data. **b**, **c** As in **a**, but for good model group and poor model group

nonlinear rectification of the HFW to the anomalous condensational heating ($\widetilde{Q_2}$). The development of the shallow convective heating in the east of the MJO deep convection is prominent and it can excess its counterpart in the west in the observation and the good model group. However, in the poor model group, the shallow convective heating in the east of the MJO deep convection grows slowly and is consistently weaker than the shallow convective heating in the west. Analyzing of the nonlinear rectification of the HFW to the MJO condensation heating, it finds that the asymmetric structures of $\widetilde{Q_{2\_T-LI}}$ and $\widetilde{Q_{2\_LH}}$ are essential to the development of the shallow convective heating of MJO. In the lower troposphere, the $\widetilde{Q_{2\_T-LI}}$ (or $\widetilde{Q_{2\_LH}}$) produces a negative (positive) anomaly in the west (east) of the MJO deep convection in the observation and the good model group. This asymmetric $\widetilde{Q_{2\_T-LI}}$ ($\widetilde{Q_{2\_LH}}$) indicates the nonlinear rectification of HFW exerts to decay the former deep convection and promote the establishment of the shallow convection in the east of MJO convection. There is no prominent asymmetric structure of $\widetilde{Q_{2\_T-LI}}$ ($\widetilde{Q_{2\_LH}}$) existing in the poor model group. The difference of the nonlinearly rectified condensational heating between the good and poor model group accounts for the largest contributor, meridional advection of specific humidity anomaly ($\widetilde{-Lv'\frac{\partial q'}{\partial y}}$). Because of the modulation of the MJO to the HFW intensity, there is weakened (enhanced) meridional wind and specific humidity anomaly of HFW in the east (west) of MJO convection, which decrease (increase) the mixing of dry air from extratropic to tropic region and contributes to the positive (negative) $\widetilde{-Lv'\frac{\partial q'}{\partial y}}$. The modulation of HFW's intensity is not significant in the east and west

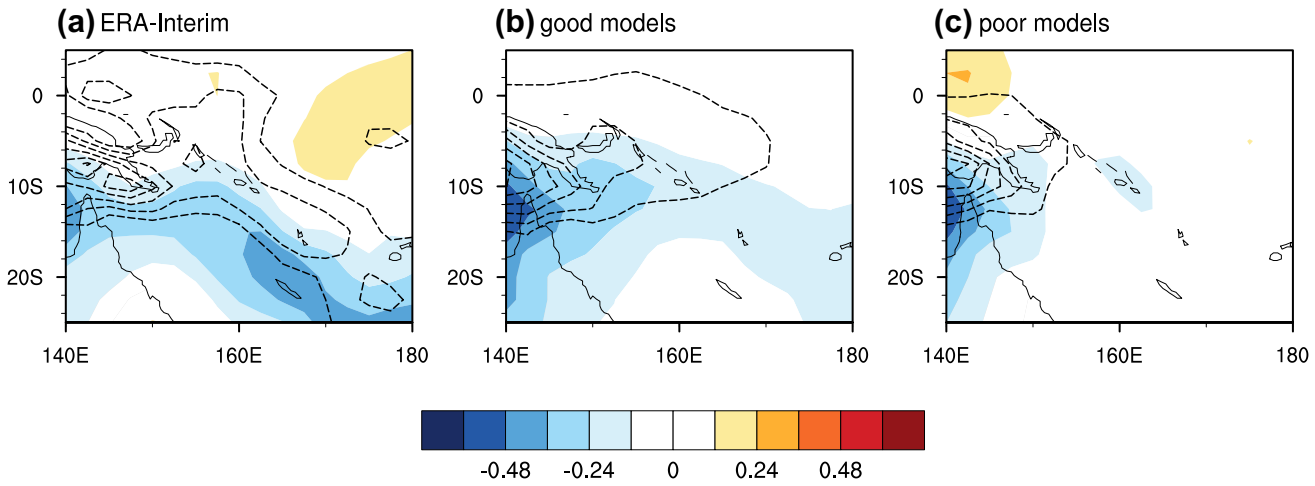

Fig. 15 The horizontal structure of $\frac{\partial \tilde{u}}{\partial x}$ (contour, unit:, s^{-1}, interval is 2×10^{-7} s^{-1} and with negative value plotted only) and $\tilde{v}$ (shading, unit: ms^{-1}) at 850-hPa for MJO active phase minus suppressed phase composite of ERA-Interim data. **b**, **c** As in **a**, but for good model group and poor model group

of the MJO convection in the poor model group, therefore $\widetilde{-Lv'\frac{\partial q'}{\partial y}}$ displays no apparent asymmetric structure.

The second type of upscale feedback is the eddy momentum transport of HFW to the MJO zonal wind tendency. The zonal wind tendency anomaly ($\frac{\partial u}{\partial t}$) in the transitional region implies the propagating tendency of the MJO zonal wind. The positive $\frac{\partial u}{\partial t}$ in the transitional region in the observation and the good model group supports the eastward propagation of MJO zonal wind. But $\frac{\partial u}{\partial t}$ shows almost zero or even negative in the poor model group, which suggests the stationary or westward propagation of zonal wind. Investigating the contribution of the intraseasonal nonlinear rectification of HFW ($\widetilde{termA}$) to $\frac{\partial u}{\partial t}$, it found that $\widetilde{termA}$ displays similar positive anomaly in the transitional region in both good and poor model group. The analogous $\widetilde{termA}$ in both good and poor model groups is related to the significant increase of the HFW intensity over the MJO convection region, and therefore they have the positive zonal eddy momentum flux anomaly ($\widetilde{u'u'}$) in this region. The divergence of $\widetilde{u'u'}$ triggers the positive zonal eddy momentum flux divergence ($-\frac{\partial u'u'}{\partial x}$) over the transitional region, which is the largest contributor to the $\widetilde{termA}$ and causes $\widetilde{termA}$ analogous in good and poor model group. The different MJO zonal wind tendencies between the good and poor model groups are explained through the no HFW involved term ($\widetilde{termB}$). The positive $\widetilde{termB}$ in the good model group further supports the eastward propagating tendency. However, negative $\widetilde{termB}$ in the poor model group almost totally offsets the positive $\widetilde{termA}$, which leads to no eastward propagation. The negative $\widetilde{termB}$ attributes to the poor simulation of the intensity of intraseasonal flows, especially east of 140° E.

With the results of this work, we want to give some enlightenments to improve the simulation of the MJO eastward propagation in the climate models. The results of this study show that the nonlinear rectification of HFW is a critical key to the eastward propagation of the MJO convection. In the future, the more effort is encouraged to devote into the better simulation of high-frequency waves (e.g., MCS, CCEW, MRG…) in the models, of which their two-way interaction with the MJO can help to improve the eastward propagation of MJO. Meanwhile, the simulation of the intensity of MJO flows can also exert an impact on eastward propagation and need to be improved.

Acknowledgements This work was supported by NSFC grant 41630423, NOAA grant NA18OAR4310298, NSF AGS-1643297, NSFC grants 41875069/41575043/41575052. This is SOEST contribution number 10848, IPRC contribution number 1415, and ESMC contribution 289.

References

Benedict JJ, Randall DA (2007) Observed characteristics of the MJO relative to maximum rainfall. J Atmos Sci 64:2332–2354

Chang C, Lim H (1988) Kelvin wave-CISK: a possible mechanism for the 30–50 day oscillations. J Atmos Sci 45:1709–1720

Chen S, Wu R, Chen W, Yu B, Cao X (2016) Genesis of westerly wind bursts over the equatorial western Pacific during the onset of the strong 2015–2016 El Niño. Atmos Sci Lett 17:384–391

Chiodi AM, Harrison DE, Vecchi GA (2014) Subseasonal atmospheric variability and El Niño waveguide warming: observed effects of the Madden–Julian oscillation and westerly wind events. J Clim 27:3619–3642

Dee DP et al (2011) The ERA-Interim reanalysis: configuration and performance of the data assimilation system. Q J R Meteorol Soc 137:553–597

Duchon CE (1979) Lanczos filtering in one and two dimensions. J Appl Meteorol 18:1016–1022

Emanuel KA (1987) An air-sea interaction model of intraseasonal oscillations in the tropics. J Atmos Sci 44:2324–2340

Grimm AM (2019) Madden–Julian oscillation impacts on South American summer monsoon season: precipitation anomalies, extreme events, teleconnections, and role in the MJO cycle. Clim Dyn 1–26

Gushchina D, Dewitte B (2012) Intraseasonal tropical atmospheric variability associated with the two flavors of El Niño. Mon Weather Rev 140:3669–3681

Hall JD, Matthews AJ, Karoly DJ (2001) The modulation of tropical cyclone activity in the Australian region by the Madden–Julian oscillation. Mon Weather Rev 129:2970–2982

Hendon HH, Wheeler MC, Zhang C (2007) Seasonal dependence of the MJO–ENSO relationship. J Clim 20:531–543

Hsu P-C, Li T (2011) Interactions between boreal summer intraseasonal oscillations and synoptic-scale disturbances over the western North Pacific. Part II: apparent heat and moisture sources and eddy momentum transport. J Clim 24:942–961

Hsu P-C, Li T (2012) Role of the boundary layer moisture asymmetry in causing the eastward propagation of the Madden–Julian oscillation. J Clim 25:4914–4931

Hsu PC, Li T, Tsou CH (2011) Interactions between Boreal Summer intraseasonal oscillations and synoptic-scale disturbances over the Western North Pacific. Part I: Energetics diagnosis*. J Clim 24:927–941

Huffman GJ et al (2001) Global precipitation at one-degree daily resolution from multisatellite observations. J Hydrometeorol 2:36–50

Hung CW, Yanai M (2004) Factors contributing to the onset of the Australian summer monsoon. Q J R Meteorol Soc 130:739–758

Hung M-P, Lin J-L, Wang W, Kim D, Shinoda T, Weaver SJ (2013) MJO and convectively coupled equatorial waves simulated by CMIP5 climate models. J Clim 26:6185–6214

Jeong J-H, Kim B-M, Ho C-H, Noh Y-H (2008) Systematic variation in wintertime precipitation in East Asia by MJO-induced extratropical vertical motion. J Clim 21:788–801

Jiang X et al (2015) Vertical structure and physical processes of the Madden–Julian oscillation: exploring key model physics in climate simulations. J Geophys Res Atmos 120:4718–4748

Kikuchi K, Wang B (2010) Spatiotemporal wavelet transform and the multiscale behavior of the Madden–Julian oscillation. J Clim 23:3814–3834

Kim D et al (2009) Application of MJO simulation diagnostics to climate models. J Clim 22:6413–6436

Klotzbach PJ (2014) The Madden–Julian oscillation's impacts on worldwide tropical cyclone activity. J Clim 27:2317–2330

Krishnamurti T, Krishnamurti R, Simon A, Thomas A, Kumar V (2016) A mechanism of the MJO invoking scale interactions. Meteorol Monogr 56:5.1–5.16

Lengaigne M, Boulanger J-P, Menkes C, Madec G, Delecluse P, Guilyardi E, Slingo J (2003) The March 1997 westerly wind event and the onset of the 1997/98 El Nino: understanding the role of the atmospheric response. J Clim 16:3330–3343

Lin J-L et al (2006) Tropical intraseasonal variability in 14 IPCC AR4 climate models. Part I: Convective signals. J Clim 19:2665–2690

Lin J-L, Lee M-I, Kim D, Kang I-S, Frierson DM (2008) The impacts of convective parameterization and moisture triggering on AGCM-simulated convectively coupled equatorial waves. J Clim 21:883–909

Liu F, Wang B (2012) A frictional skeleton model for the Madden–Julian oscillation. J Atmos Sci 69:2749–2758

Liu F, Wang B (2013) Impacts of upscale heat and momentum transfer by moist Kelvin waves on the Madden–Julian oscillation: a theoretical model study. Clim Dyn 40:213–224

Madden RA, Julian PR (1971) Detection of a 40–50 day oscillation in the zonal wind in the tropical Pacific. J Atmos Sci 28:702–708

Madden RA, Julian PR (1972) Description of global-scale circulation cells in the tropics with a 40–50 day period. J Atmos Sci 29:1109–1123

Majda AJ, Stechmann SN (2009) The skeleton of tropical intraseasonal oscillations. Proc Natl Acad Sci 106:8417–8422

Maloney ED (2009) The moist static energy budget of a composite tropical intraseasonal oscillation in a climate model. J Clim 22:711–729

Maloney ED, Dickinson MJ (2003) The intraseasonal oscillation and the energetics of summertime tropical western North Pacific synoptic-scale disturbances. J Atmos Sci 60:2153–2168

Nakazawa T (1988) Tropical super clusters within intraseasonal variations over the western Pacific. J Meteorol Soc Japan Ser II 66:823–839

Neelin JD, Held IM, Cook KH (1987) Evaporation-wind feedback and low-frequency variability in the tropical atmosphere. J Atmos Sci 44:2341–2348

Oh J-H, Kim K-Y, Lim G-H (2012) Impact of MJO on the diurnal cycle of rainfall over the western Maritime Continent in the austral summer. Clim Dyn 38:1167–1180

Pai D, Bhate J, Sreejith O, Hatwar H (2011) Impact of MJO on the intraseasonal variation of summer monsoon rainfall over India. Clim Dyn 36:41–55

Peatman SC, Matthews AJ, Stevens DP (2014) Propagation of the Madden–Julian oscillation through the Maritime Continent and scale interaction with the diurnal cycle of precipitation. Q J R Meteorol Soc 140:814–825

Rauniyar SP, Walsh KJ (2011) Scale interaction of the diurnal cycle of rainfall over the Maritime Continent and Australia: influence of the MJO. J Clim 24:325–348

Singh S, Kripalani R, Sikka D (1992) Interannual variability of the Madden–Julian oscillations in Indian summer monsoon rainfall. J Clim 5:973–978

Sobel AH, Maloney ED (2000) Effect of ENSO and the MJO on western North Pacific tropical cyclones. Geophys Res Lett 27:1739–1742

Sobel A, Maloney E (2012) An idealized semi-empirical framework for modeling the Madden–Julian oscillation. J Atmos Sci 69:1691–1705

Sobel A, Maloney E (2013) Moisture modes and the eastward propagation of the MJO. J Atmos Sci 70:187–192

Wang B (1988) Dynamics of tropical low-frequency waves: an analysis of the moist Kelvin wave. J Atmos Sci 45:2051–2065

Wang B, Chen G (2017) A general theoretical framework for understanding essential dynamics of Madden–Julian oscillation. Clim Dyn 49:2309–2328

Wang B, Lee S-S (2017) MJO propagation shaped by zonal asymmetric structures: results from 24 GCM simulations. J Clim 30:7933–7952

Wang B, Li T (1994) Convective interaction with boundary-layer dynamics in the development of a tropical intraseasonal system. J Atmos Sci 51:1386–1400

Wang B, Liu F (2011) A model for scale interaction in the Madden–Julian oscillation. J Atmos Sci 68:2524–2536

Wang B, Xie X (1996) Low-frequency equatorial waves in vertically sheared zonal flow. Part I: Stable waves. J Atmos Sci 53:449–467

Wang L, Li T, Maloney E, Wang B (2017) Fundamental causes of propagating and nonpropagating MJOs in MJOTF/GASS models. J Clim 30:3743–3769

Wheeler MC, Hendon HH, Cleland S, Meinke H, Donald A (2009) Impacts of the Madden–Julian oscillation on Australian rainfall and circulation. J Clim 22:1482–1498

Yanai M, Esbensen S, Chu J-H (1973) Determination of bulk properties of tropical cloud clusters from large-scale heat and moisture budgets. J Atmos Sci 30:611–627

Zhou C, Li T (2010) Upscale feedback of tropical synoptic variability to intraseasonal oscillations through the nonlinear rectification of the surface latent heat flux. J Clim 23:5738–5754

Zhu H, Hendon H, Jakob C (2009) Convection in a parameterized and superparameterized model and its role in the representation of the MJO. J Atmos Sci 66:2796–2811

Zhu Y, Li T, Zhao M, Nasuno T (2019) Interaction between MJO and high frequency waves over Maritime Continent in Boreal Winter. J Clim